MDPI

Article

Thermo-Mechanical Study of TIG Welding of Ti-6Al-4V for Residual Stresses Considering Solid State Phase Transformation

Jingang Liu, Jianyun Zheng *, Bing Fu, Lei Bu, Ruiqi Li and Songye Liu

School of Mechanical Engineering, Xiangtan University, Xiangtan 411105, China
* Correspondence: 202031000189@smail.xtu.edu.cn

Abstract: To overcome the detrimental effect of residual stress in welded joints, which affects the overall performance of the welded structure, this paper studies the magnitude and distribution of residual stress after welding and local post-weld heat treatment (PWHT). The coupled thermo-metallurgical-mechanical model for welding 6 mm thick Ti-6Al-4V (TC4) titanium alloy plates was established, the evolution of the SSPT and its effect on the residual stress were quantitatively analyzed, and a parametric analysis of local PWHT was performed. The results demonstrated that there was good agreement between the numerical results and the experimental data. Due to the cooling rate reaching 327 °C/s, the volume fraction of $\alpha`$ in the fusion zone (FZ) reached 0.218 after welding and decreased by 90.83% after PWHT when the heating temperature was 700 °C. The peak value of the longitudinal residual stress can reach 686.4 MPa after welding with SSPT, which was 11.38% lower than that without SSPT, and it decreased by 65.6% after PWHT when the heating temperature was 900 °C. The research results demonstrate that SSPT has a significant effect on residual stress, and PWHT can obviously reduce the residual stress, which provides a certain reference for welding TC4 titanium alloy plates.

Keywords: titanium alloy; welding; phase transformation; residual stress; heat treatment

check for **updates**

1. Introduction

Ti-6Al-4V (TC4) titanium alloy has significant advantages such as low density, high strength, corrosion resistance, and creep properties, and it has been widely used in medical equipment, shipbuilding, and automobile manufacturing industries [1,2]. Some special vehicles have relatively high requirements for light weight and strength, and TC4 titanium alloy has become a very promising application material for these vehicle bodies. However, due to the poor thermal conductivity and susceptibility to oxidation at high temperatures, the welding of TC4 titanium alloy plates for special vehicles requires special processes. Many advanced and efficient joining technologies for TC4 titanium alloy structures have been developed and applied, among which electron beam welding and laser welding have the advantages of fast welding speeds and narrow heat-affected zones of welds [3–5]. However, TC4 titanium alloy sheets have low absorption by the laser, and electron beam welding of titanium alloy needs to be carried out in a specific vacuum environment, making the two processes inefficient and expensive for specific applications. On the contrary, TIG welding is suggested as an economical and effective alternative to laser welding and electron beam welding [6]. However, for the TIG welding process, non-uniform thermal expansion and contraction during welding result in huge tensile residual stress in the weld and its vicinity, which will affect the overall performance of the welded joint.

Residual stress is a fatal factor affecting the fatigue performance and stress corrosion resistance of welded joints. Yet, it is considered that local PWHT could be employed to relieve residual stress but cannot completely eliminate it. In recent years, many scholars have studied the variations in microstructure, mechanical properties, and residual stress

of weldments after welding and heat treatment through experiments. Chen et al. [7] and Kumar et al. [8] analyzed the microstructure of titanium alloy welds and found that due to the transformation of the initial α + β phase to α and martensite during the cooling process, the hardness value in the weld was larger than that of the base metal. To better analyze the microstructure and residual stresses in TC4 titanium alloy pulsed and unpulsed TIG welds, Mehdi et al. [9] carried out some experiments, finding that the increase of the pulse frequency from 1 Hz to 5 Hz reduced the magnitude of the tensile residual stresses in the heat-affected zone (HAZ) and weakened the compressive ones in the fusion zone (FZ). The literature on Etesami et al. [10] noticed that aging heat treatment can be used to lower residual stress and also reduce the deformation of TC4 parts during the laser-based powder-bed fusion (L-PBF) additive manufacturing process, but could not significantly alter the strength and ductility of welded joints. Bagheri et al. [11] studied the use of different welding methods to connect billets with different characteristics and form a tailor-welded blank (TWB) and found that the forming limit diagram (FLD) for TWBs made by friction stir welding (FSW) is higher than FLD for TWBs made by CO2 laser welding, and FLD_0 for TWBs made by friction stir vibration welding (FSVW) increases as vibration frequency increases. Nie et al. [12] reviewed the research progress of cutting imaging technology, analyzed the important physical quantities of the chip formation process obtained from cutting imaging, revealed the advantages and importance of cutting imaging, and looked forward to its future development direction.

With the continuous development of computer technology and simulation software, numerical simulation methods can more cost-effectively predict the evolution of temperature and transient stress during welding and heat treatment, as well as the magnitude and distribution of residual stress after welding and heat treatment. Chen et al. [13] investigated the effect of component radius to wall thickness ratio (r/t) and heat input on the welding stress profile. Results showed that the hoop membrane stress at a weld toe gradually increased with the r/t ratio, while the hoop and axial bending stresses at a weld toe decreased with the r/t ratio. The academic literature on Kumar et al. [14] revealed the influence of low carbon steel plasma-assisted friction stir welding (P-FSW) process parameters on the peak temperature by simulation and experiment and mentioned that preheating can significantly refine the grains inside the stir zone, which enhanced the tensile strength of the P-FSW samples more than the friction stir welding samples. Luo et al. [15] carried out a numerical simulation of the local PWHT process after welding of the super-large pressure vessel, and the results presented showed that the local PWHT can reduce the hoop and axial stress in the welded joint. In addition, they also found both the von-misese equivalent stress and the maximum principal stress were reduced, especially at the weld toe, thereby reducing the risk of cracking. The investigations of Hu et al. [16] discussed the influence of pipe dimensions, including pipe diameter and pipe thickness, on the temperature field during heat treatment of heavy-wall 9% Cr heat-resistant steel pipes and found that with the increase of pipe diameter and pipe thickness, the temperature gradient of weldments along the depth and thickness also increased. Based on the Taguchi method, Bagheri et al. [17] investigated the optimal process parameters of AA6061-T6 aluminum alloy FSW and implemented simulation by a coupled Eulerian and Lagrangian technique, finding that the application of optimal joining conditions can decrease the peak tensile residual stress by about 38.3%. Abdollahzadeh et al. [18] analyzed the pinless friction stir spot welding of aluminum-copper composite with Zn interlayer under experimental measurement and the finite element method, and the research results indicated that the heat source, due to plastic deformation and friction, increased as the shoulder diameter was increased, whereas the stress distribution in the weld samples was reduced. Furthermore, they also observed that the axial compressive stresses showed the lowest profile as the shoulder diameter of the tool is 16 mm.

From the literature review, various researchers have put forth commendable efforts, which make a certain contribution to the reduction of residual stress and also provide a reference for this work. However, researchers usually analyze the microstructure of weld-

ments through experiments, which is costly and time-consuming. Moreover, experimental methods may not be able to visually observe the evolution of microstructure in high-temperature areas during the welding process, and there is a lack of research on the relationship between temperature and microstructure evolution as well as the impact of SSPT on residual stress. In addition, quantitative analyses of residual stress reduction and redistribution characteristics in weldments after PWHT are also rarely reported.

In this work, based on the thermo-elasto-plastic analysis theory, a welding finite element simulation model of 6 mm thick TC4 titanium alloy plates was established. It was employed to study the magnitude and distribution of residual stress after multi-layer multi-pass TIG welding and local PWHT. In order to accurately predict the residual stress, the effect of the SSPT of the material was considered, and its evolution was quantitatively analyzed. A double ellipsoid heat source was used to simulate the heat input of the TIG welding, and the effect of the molten pool flow on the heat transfer was also considered by increasing the thermal conductivity value in the weld. The local PWHT was utilized to reduce the residual stress, and the correctness and effectiveness of the simulation model were verified by means of experiments.

2. Experiments and Measurement

2.1. Materials and Procedures

The materials considered in this investigation were 6 mm thick TC4 titanium alloy plates (Dongguan Jiejin Metal Material Co., Ltd., Dongguan, China) with a dimension of 150 mm × 75 mm × 6 mm, and the chemical composition could be obtained by referring to the relevant literature [19]. The material of the selected welding wire was the same as that of the base metal, and the diameter of the welding wire was 2.4 mm. The type of bevel was V-shaped, and the bevel angle was 70° with a blunt edge of 1.6 mm and a reserved gap of 3 mm, as detailed in Figure 1b. Before the test, the experimental set-up for multi-layer, multi-pass TIG welding of TC4 titanium alloy plates was built, as shown in Figure 1a, and the areas to be welded and other areas of the TC4 titanium alloy plate were de-oxidized and decontaminated. During the test, the test specimens were fixed with a C-type fixture to constrain the rigid body's movement in the vertical direction. The YC-300WX Panasonic AC and DC TIG welding machine (Panasonic Welding Systems (Tangshan) Co., Ltd., Tangshan, China) was used to perform multi-layer multi-pass butt welding, and the surface and bottom of the weld were protected by argon gas during the welding process. The number of the welding layers is shown in Figure 1b, and the process parameters required for the welding test in this work are given in Table 1.
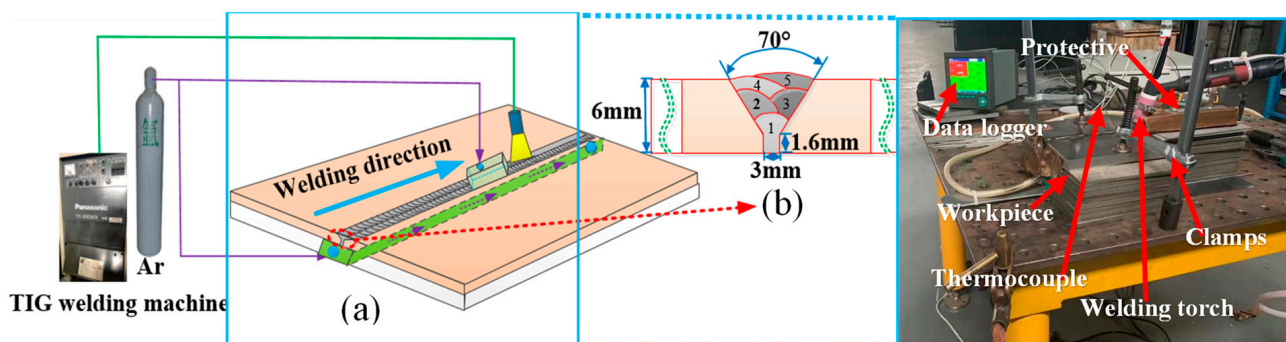

Figure 1. (**a**) TIG welding experimental set-up and (**b**) schematic of welding sequence and groove shape.

Table 1. Welding parameters.

Parameters	Value/Unit
Basic current	40 A
peak current	140 A
Voltage	12 V
Pulse frequency	5 Hz
wire feed speed	1 mm/s
Welding speed	4 mm/s
Argon gas flow	11 L/min

2.2. Measurement of Thermal History and Molten Pool Morphology

In order to obtain the temperature distribution near the weld during the welding, multi-channel K-type thermocouples (Hangzhou Sinomeasure Automation Technology Co., Ltd., Hangzhou, China) were employed and spot-welded on the top side of the plate, and the distances from the weld center to these three observation points were 5.5 mm, 7.5 mm, and 9.5 mm, respectively, as shown in Figure 2. The thermocouples were used to measure welding thermal histories during the TIG welding process, and a thermocouple input module was utilized to record the temperature data. After welding, in order to observe the cross-sectional profile of the welded joint, the welded specimen was cut in the direction perpendicular to the welding seam to obtain metallographic samples. Then, these samples were polished and etched with Kroll's reagent (2% HF, 2% HNO3, and 96% distilled water) for 6 s. The cross-sectional morphology of the weld was observed through an optical microscope (GRG Metrology & Test Group Co., Ltd., Guangzhou, China), and the microstructure of the weld was also examined.
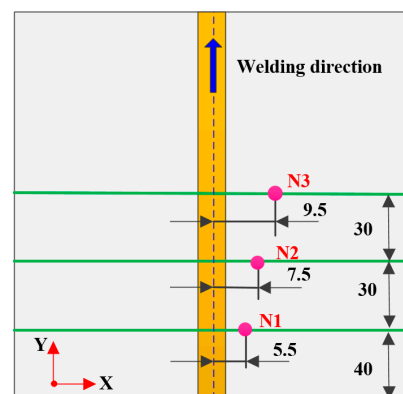
Figure 2. Arranged location of thermocouples (units in mm).

2.3. Measurement of Residual Stress

In this research, the blind hole method was employed to measure the magnitude of residual stress on the top side of the welded joint, and the experimental results were used to verify the correctness and validity of the simulation model. The working principle of the blind hole method is shown in Figure 3. It could be seen that three strain gages (R_1, R_2, and R_3) were required, two of which were perpendicular to each other and the third at 45°or 135° to either of the first two. When measuring the residual stress, the installation direction of two mutually perpendicular strain gauges must be parallel or perpendicular to the weld. The principal stresses σ_1 and σ_2 and the angle θ between the principal stress directions were calculated from the strain values (ε_1, ε_2, ε_3) measured by three strain gauges (Wuhan Jingze Technology Co.,Ltd., Wuhan, China), and the formulas were as follows in Equations (1) and (2) [20].

$$\left.\begin{array}{c}\sigma_1\\\sigma_2\end{array}\right\} = \frac{\varepsilon_1 + \varepsilon_3}{4A} \mp \frac{1}{4B}\sqrt{(\varepsilon_1 - \varepsilon_3)^2 + (\varepsilon_1 + \varepsilon_3 - 2\varepsilon_2)^2} \qquad (1)$$

$$\theta = \frac{1}{2} arctan\left(\frac{\varepsilon_1 + \varepsilon_3 - 2\varepsilon_2}{\varepsilon_1 - \varepsilon_3}\right) \tag{2}$$

where ε_1, ε_2, and ε_3 represent the released strains measured by strain gauges R_1, R_2, and R_3, respectively; θ is the angle between σ_1 and R_1; and A and B denote strain release factors, which could be calibrated by experimental tests or simulations.
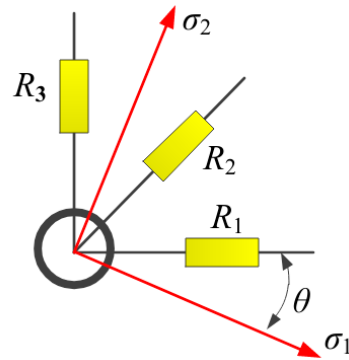
Figure 3. Schematic diagram of the working principle of the blind hole method.

3. Numerical Simulation

3.1. Finite Element Model

In the present work, a numerical study of residual stress after TIG welding and local PWHT was performed using SYSWELD (ESI, Paris, France). According to the actual size of the weldments, their geometric model was depicted in Figure 4a, and a three-dimensional welding finite element model was also established. In order to take into account the calculation speed and accuracy, the meshes in FZ and HAZ were refined, while the meshes in the remaining area were coarsened, as shown in Figure 4b. The number of 3D elements and nodes in this model was 93,950 and 107,678, respectively. During welding and local PWHT, the thermal and mechanical properties of the material changed with temperature and were obtained by interpolating and extrapolating the low-temperature performance parameters [21,22], as observed in Figure 5. The residual stresses on different observation paths in the weldments were investigated and analyzed in this work, and these paths were mainly divided into three parts. The first part included the observation paths P1, P2, P3, and P4 on the top side of weldments, and their distances away from the weld centerline were 0 mm, 5.5 mm, 7.5 mm, and 10.4 mm, respectively. The second part included the observation paths P5, P6, P7, and P8 on the bottom side of weldments, and their distances away from the weld centerline were 0 mm, 5.5 mm, 7.5 mm, and 10.4 mm, respectively. Additionally, the last part included the observation path P9 on the top side of the weldments and the observation path P10 on the bottom side of the weldments, both of which are 80 mm away from the welding starting position, as shown in Figure 4a.
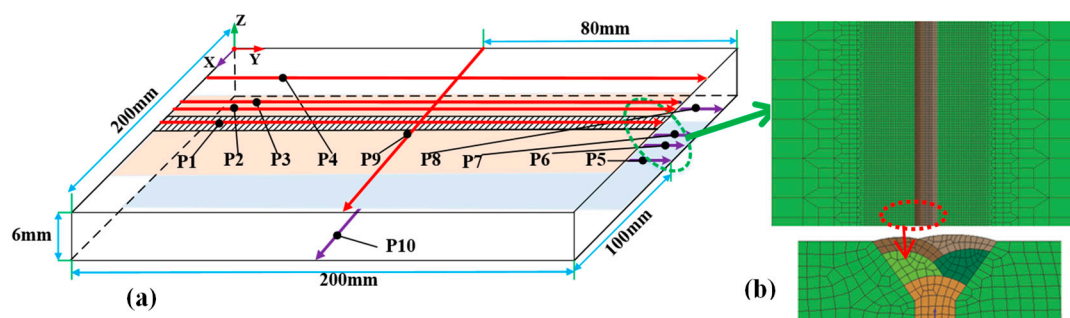
Figure 4. Schematic diagram of the (**a**) geometric model and (**b**) mesh model of the weldments.
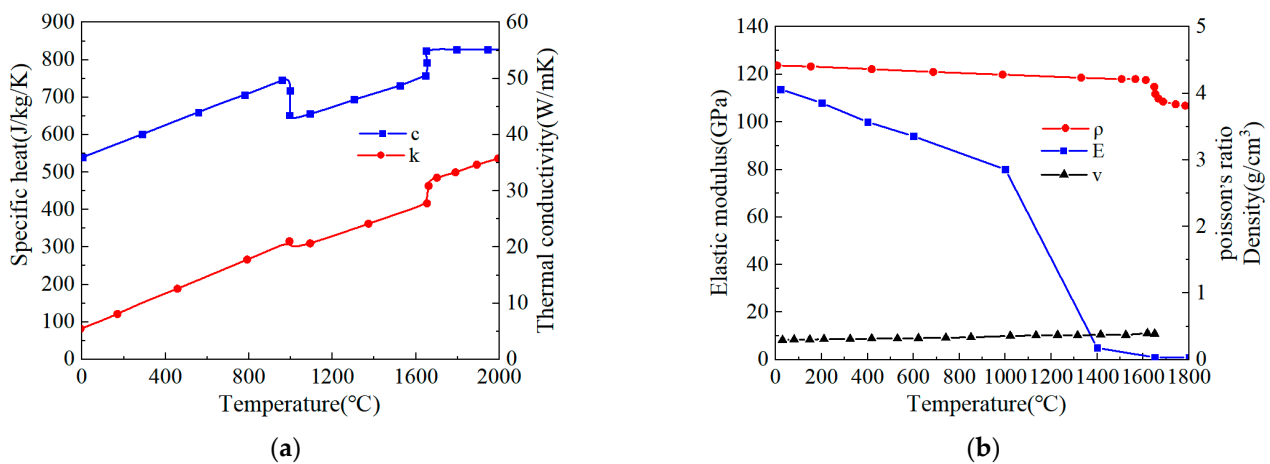
Figure 5. Temperature-dependent (**a**) thermo-physical and (**b**) thermo-mechanical material properties of Ti-6Al-4V used in the finite element model.

3.2. Heat Source Model

At present, the typical heat source models include point heat source models, Gaussian heat source models, double ellipsoid heat source models, and other heat sources with relatively single shapes, as well as combined heat source models that combine two or more heat sources, etc. In this study, considering relative factors such as the shape of the molten pool and distribution characteristics of heat flow during welding, the double ellipsoid power density distribution heat source model proposed by Goldak was selected [23,24]. The double ellipsoid heat source model includes two parts, the front and the rear, as shown in Figure 6. For the heat flux density $Q(x, y, z)$ at a point (x, y, z) in the heat source model, it can be expressed by Equation (3).

$$Q(x, y, z, t) = \frac{6\sqrt{3}fQ_E}{abc\pi\sqrt{\pi}}e^{\left(-\frac{3x^2}{a^2} - \frac{3(y-v\cdot t)^2}{b^2} - \frac{3z^2}{c^2}\right)} \tag{3}$$

where x, y, and z denote the local coordinates of the reconstructed models; v is welding speed at any instant of time (t); a, b, and c represent the geometric parameters of the heat source model in the directions of width, length, and depth, respectively; and b is further divided into b_f and b_r, which denote the radius at the front and rear ellipsoids of the heat source, respectively; Q_E represents the heat input of the heat source; f represents the proportion of energy, and f is also further divided into f_f and f_r, which denote the proportional coefficients at the front and rear ellipsoids of the heat source, respectively ($f_f + f_r = 2$) [25]. The geometric parameters of the double ellipsoid heat source model were set according to the geometrical dimensions of the weld cross-section obtained by the test, and the heat source was verified using the heat source verification tool in SYSWELD.
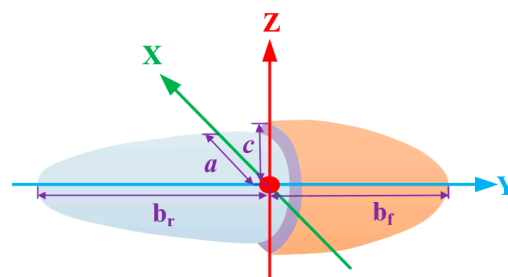

Figure 6. Schematic diagram of the double ellipsoid heat source model.

3.3. Solid-State Metallurgical Phase Transformations

The solid-state phase transformation (SSPT) in the weldments occurs during the welding heating and cooling processes, and the volume change induced by SSPT will affect the residual stress after welding. For the material model in this investigation, the transformation of the initial mixed phase (α + β) to the β phase during the heating process and the transformation of the β phase to the α phase and to the α` phase during the cooling process were defined. Since the volume fraction of the β phase in the base metal is very small, the initial mixed phases were assumed to be a single α phase and the fraction of the β phase increased by the equivalent amount of dissolution of the α phase during the heating process. Moreover, it was presumed that the transformation from the α phase to the β phase follows the modified Avrami function equation-based Weibull probability distribution function of temperature growth. Then, the transformation of α phase to β phase during the heating process could be expressed as the following equation [26]:

$$f_{\alpha \to \beta}(t_1, T_1) = 1 - \exp\left[K_{\alpha \to \beta} \left(\frac{T_1 - T_{\alpha \to \beta}}{T_\varphi - T_{\alpha \to \beta}} \right)^{\gamma_{\alpha \to \beta}} \right] (T_\beta \geq T_1 \geq T_{\alpha \to \beta}) \quad (4)$$

where $f_{\alpha \to \beta}$ denotes the phase fraction of the β phase transformed from the α phase when the temperature is T_1 during the heating process; $K_{\alpha \to \beta}$ and $\gamma_{\alpha \to \beta}$ represent material constants; $T_{\alpha \to \beta}$ and T_β represent the phase transition start temperature and phase transition end temperature of the β phase, respectively.

Due to different cooling rates, different types of phase transformations would occur during the cooling process. When the cooling temperature is lower than the transition temperature of the β phase and the cooling rate is less than 20 °C/s, the high-temperature β phase would start to decompose at the primary β grain boundary, where the α phase would be generated through nucleation and diffusion control. For simplicity, it was assumed that the α phase in this investigation ignored its different morphology, including globular, Widmanstatten, basket weave, and grain boundary α phases. Therefore, it was presumed that the transformation from β phase to α phase follows the Johnson, Mehl, Avrami, and Kolmogorov (JMAK) law as a function of temperature. Then, the transformation of β phase to α phase during the cooling stage could be expressed as the following equation [21,27].

$$f_{\beta \to \alpha}(t_2, T_2) = [1 - \exp(-K_{\beta \to \alpha}(T) t^{n_{\beta \to \alpha}})] f_\alpha^{eq}(T) \quad (5)$$

where $f_{\beta \to \alpha}$ represents the phase fraction of the α phase transformed from the β phase when the temperature is T_2 during the cooling process; $K_{\beta \to \alpha}$ and $n_{\beta \to \alpha}$ represent the temperature-dependent and independent JMAK parameters that determine the kinetics of the β phase; f_α^{eq} represent the equilibrium fraction of the α phase. When the peak value of the heating temperature reaches above the transition temperature of the β phase and the cooling rate is between 20 °C/s and 410 °C/s during the cooling process, there would be partial transformation of β phase to grain boundary α_G phase and α′ phase adjacent to the prior-β grain boundary, and it was assumed that α_m includes both α_G and α′ and also that both transformations are diffusional and diffusionless [18]. Then, the transformation of β phase to α_m phase during the cooling process could be expressed as Equation (6).

$$f_{\alpha_m}(t_3, T_3) = f_{\alpha_m}(t_0, T_0) + \Delta f_{\alpha_m} = [1 - \exp(-K_{\beta \to \alpha_m}(M_s - T))] \times \left(f_\beta(t_0, T_0) + f_{\alpha_m}(t_0, T_0) - f_\beta^{eq}(T_3) \right) \quad (6)$$

where f_{α_m} represents the phase fraction of the α_m phase transformed from the β phase when the temperature is T_3 during the cooling process; f_β^{eq} denotes the equilibrium fraction of the β phase. When the cooling rate is greater than 410 °C/s, martensitic transformation occurs dominantly, and the formation of martensite is a non-diffusion or displacement solid-state phase transition that rapidly changes the crystal structure without rearranging the atoms. Similarly, it was assumed that the fraction of α` phase increased by the

equivalent amount of dissolution of the β phase, and it was assumed that the martensitic transformation follows the Koistenen–Marburger formulation [28,29], which is expressed as Equation (7).

$$f_{\beta \to \alpha}(t_3, T_3) = 1 - \exp[-K_{\beta \to \alpha}(T_{\beta \to \alpha} - T_3)] \cdot f_\beta \,(T_\alpha \leq T_3 \leq T_{\beta \to \alpha}) \tag{7}$$

where $f_{\beta \to \alpha}$ represents the phase fraction of the $\alpha\text{\`}$ phase transformed from the β phase when the temperature is $T_3$ during cooling; $K_{\beta \to \alpha}$ is the material constant; $T_{\beta \to \alpha}$ denotes the phase transition start temperature of the $\alpha\text{\`}$ phase; T_α represents the phase transition end temperature of the $\alpha\text{\`}$ phase.

In order to examine the influence of SSPT on residual stress, one simulation case did not consider the effect of SSPT during welding finite element analysis, while the other simulation case considered the effect of SSPT. However, the finite element mesh model, welding process parameters, thermal and mechanical initial conditions, and boundary conditions were the same for both simulation cases. Finally, the effect of SSPT on residual stress was investigated by analyzing the longitudinal and transverse residual stresses on the observation paths P9 and P10 on the weldments.

3.4. Governing Equations and Boundary Conditions

In the process of welding and local PWHT, energy is input to the surface of the weldments and then transferred to other regions of the weldments in the form of heat conduction. This process is a typical nonlinear transient heat conduction problem [30]. The temperature distribution in the whole workpiece during the welding process can be calculated by the resolution of the nonlinear transient heat transfer equation, as shown in the following Equation (8). Furthermore, the heat losses caused by natural convection and radiation are regarded as thermal boundary conditions and could be defined by Equations (9) and (10), respectively.

$$\nabla(k\nabla T) + Q(x, y, z, t) = \rho c_p \left(\frac{\partial T}{\partial t} \right) \tag{8}$$

$$q_{conv} = h_{conv}(T - T_0) \tag{9}$$

$$q_{\text{rad}} = \varepsilon \sigma \left[(T - T_{\text{abs}})^4 - (T_0 - T_{\text{abs}})^4 \right] \tag{10}$$

where $Q\,(x, y, z, t)$ is the intensity of the internal heat source at different positions of the weldments at any instant of time (t); T represents the transient temperature; ρ means the density; c denotes the specific heat capacity; k represents the thermal conductivity; h_{conv} is the heat transfer coefficient; T_0 means the ambient temperature, which is set at 25 °C; T_{abs} denotes the absolute zero temperature; ε represents the emissivity; σ is the Stefan Boltzmann constant (5.67×10^{-8} W·K^{-4}·m^{-2}). In addition, the equilibrium equation and thermo-elasto-plastic constitutive equation are also defined as follows:

$$\nabla \sigma + F = 0 \tag{11}$$

$$\{d\sigma\} = ([D^{\text{e}}] + [D^{\text{p}}])\{d\varepsilon\} - \{C\}dT \tag{12}$$

$$\Delta \varepsilon = \Delta \varepsilon_e + \Delta \varepsilon_p + \Delta \varepsilon_{th} + \Delta \varepsilon_{vol} \tag{13}$$

where σ is the stress component; F represents the volume force; $[D^{\text{e}}]$ and $[D^{\text{p}}]$ mean the elastic stiffness matrix and the plastic stiffness matrix; $\{C\}$ denotes the thermal stiffness matrix; $\Delta \varepsilon$ is the total strain increment; $\Delta \varepsilon_e$ denotes the elastic strain increment; $\Delta \varepsilon_p$ is the plastic strain increment; $\Delta \varepsilon_{th}$ represents the thermal strain increment; $\Delta \varepsilon_{vol}$ is the volumetric strain increment. The yield criterion follows the Von Mises criterion, and the strain hardening of the material adopts the isotropic hardening model. At the same time, the actual clamping conditions in the test are simulated by applying mechanical boundary conditions to limit the rigid body movement of the weldments in the vertical direction.

After the weldments were cooled to room temperature, the local PWHT was performed on the weld and its vicinity to reduce the residual stress. In order to study the influence of local PWHT on the residual stress in detail, the process parameters of local PWHT were further analyzed, and the holding time and holding temperature were the critical factors affecting the residual stress. Therefore, in this work, several different cases were analyzed by numerical simulation. When studying the effect of holding time on residual stress relaxation, the holding temperature was kept at 700 °C, and the holding time varied from 1 h to 5 h. When studying the influence of holding temperature on residual stress relaxation, the holding time was kept at 3 h, and the holding temperature varied from 500 °C to 800 °C. It was worth noting that the holding temperature of all cases should definitely be less than the phase transition start temperature of the β phase, the heating rate v was 45 °C/min, and the cooling method was air cooling. The curve of local PWHT is shown in Figure 7.
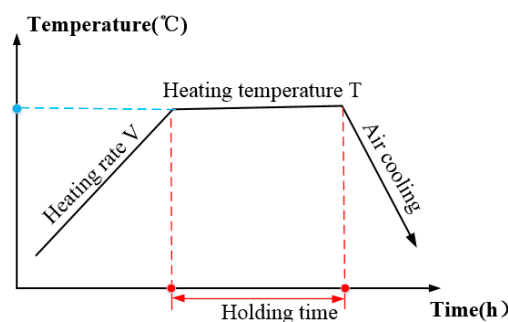

Figure 7. Schematic illustration of the local PWHT cycle.

4. Results and Discussion

4.1. Thermal Analysis

In thermal simulation analysis, since the melting point for TC4 titanium alloy is 1665 °C, the isotherm with a temperature of 1665 °C can be used as the boundary line of the solid-liquid interface, and the region of temperature above 1665 °C in the temperature field can be regarded as the molten pool. Figure 8 clearly represents the weld transverse cross-section morphology obtained from experimental and simulated results.
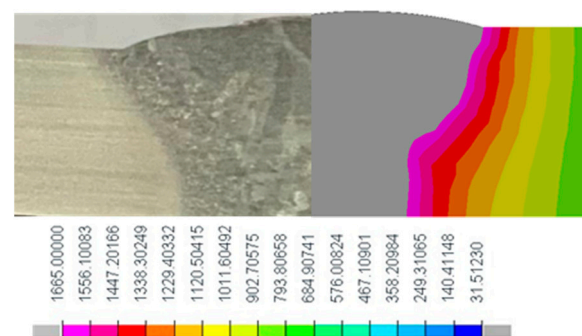

Figure 8. Comparison of weld transverse cross-section geometry and morphology between simulated and experimental results.

Figure 9a shows the measured and simulated thermal cycles for the first welding pass in the welded joint. By comparing the values of the heating rate, peak temperature, and cooling rate at three observation points (N1, N2, and N3), respectively, it can be concluded that the simulated results matched the trend of the measured thermal cycles generally. Additionally, there was also a small error between the temperature peaks obtained from the simulation and the experiment, which may be attributed to the heat source model and the measurement method. Overall, it can be shown that the model established in this research

was correct and effective and can be used for the subsequent mechanical simulation analysis of residual stress.
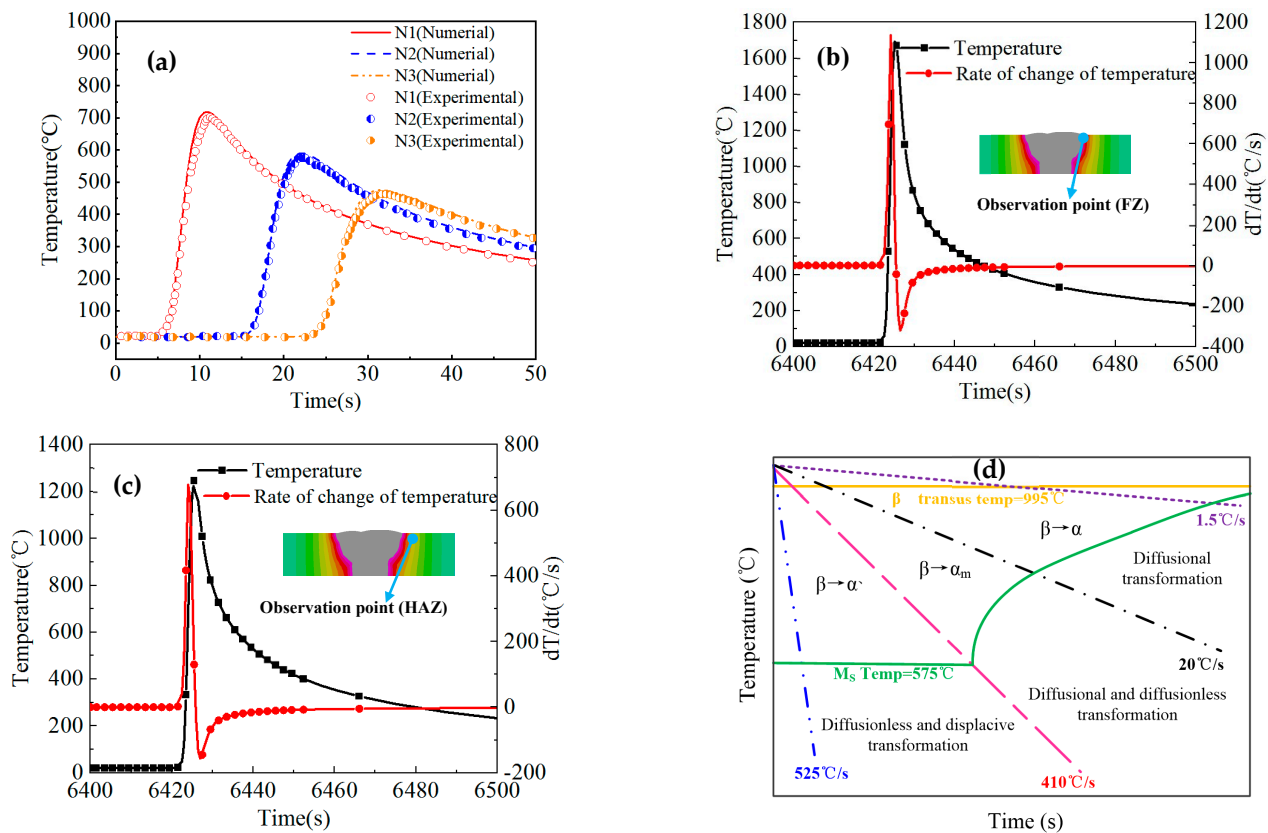

Figure 9. (**a**) Comparison of the calculated and measured thermal cycles for the 1st welding pass; (**b**) relation between temperature history and rate of change of temperature at an observation point in FZ near the fusion line for the last welding pass; (**c**) relation between temperature history and rate of change of temperature at an observation point in HAZ for the last welding pass; and (**d**) schematic continuous cooling diagram for TC4.

In Figure 9b, it can be seen that the peak temperature of the target point in FZ near the fusion line had reached the melting point of the material for the last welding pass, and its maximum cooling rate was about 327 °C/s in the range of 20 °C/s and 410 °C/s during the cooling process, which would lead to the diffusional and diffusionless transformations according to Figure 9d [8,31]. On the other hand, according to Figure 9c, the peak temperature of the target point in HAZ can reach 1222 °C, which is greater than the β phase transus temperature but less than the melting point of the material, and its maximum cooling rate during cooling was 154 °C/s and was smaller than that in FZ, which may make the transus temperature, morphology, and content of α` phase different from those in FZ.

4.2. Metallurgical Analysis

The changes of various phases in the FZ and HAZ of weldments during heating and cooling were quantitatively studied through simulation analysis. At the same time, the change of phase in the FZ during local PWHT was also discussed, and that in the HAZ during local PWHT will not be discussed further here due to its small change. Figure 10a,b shows the simulated variations in the volume fractions of α, β, and α` phases at observation points in the FZ and HAZ of weldment during welding, respectively, and Figure 10c shows the simulated variations in the volume fractions of α, β, and α` phases at an observation point in the FZ near the fusion line of weldment during local PWHT at 700 °C for 3 h.
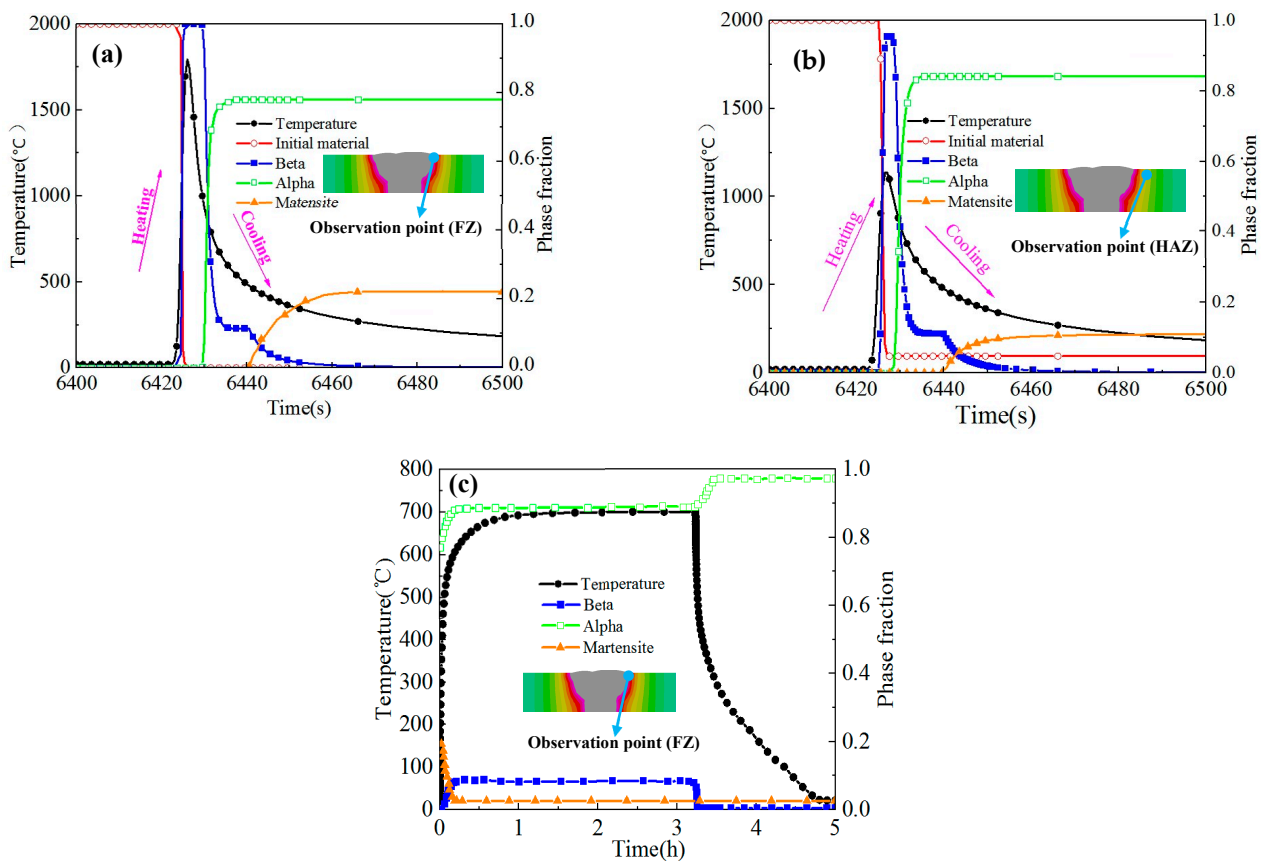
Figure 10. Time-temperature history and volume fractions of microconstituents for observation points in the (**a**) FZ and (**b**) HAZ of the weldment for the last welding pass and that in the (**c**) FZ during local PWHT at 700 °C for 3 h.

According to Figure 10a, when the temperature quickly increased to a certain value due to the high heating rate during the welding heating process, the initial phase rapidly dissolved, and the high-temperature β phase also began to form, and its volume fraction reached 1 above the transus temperature of the β phase. During the cooling process, as the temperature dropped to a certain value, the high-temperature β phase began to be decomposed continuously, and the α phase was first generated, and its volume fraction can reach 0.76 eventually. Then, when the weldment continued to cool to martensite transus temperature, α` phase began to generate, and its volume fraction can reach 0.218 after cooling to room temperature, which is obviously less than that of the α phase. Furthermore, according to Figure 10b, it was found that the initial phase (α + β) in the HAZ was not completely transformed into the high-temperature β phase compared with that in the FZ, and the volume fraction of martensite phase generated in the HAZ after cooling to room temperature was very small and also less than that in the FZ.

Furthermore, as shown in Figure 10c, with the temperature reaching 700 °C again, the α` phase at the target point was partially decomposed into the α phase and the β phase, and its volume fraction was only about 0.02 at the end. Some of the β phase was generated during heating, and most of it was converted into the α phase again during subsequent cooling to room temperature, with a small fraction of it eventually remaining, while the α phase increased in the heating and cooling process of local PWHT, and its volume fraction reached about 0.97 after cooling to room temperature, which will affect the mechanical properties of welded joints. The discovery in this simulation analysis that the decomposition of α′→α + β occurred during local PWHT also appeared in the results obtained by the researchers through experiments [32–34].

Figure 11 shows the morphology of the prior-β grain and the distribution of microstructure in the cross-section of the welded joint obtained from the test. As shown in Figure 11a, due to the large temperature gradient in FZ, a larger size of prior-β grain appeared in FZ and grew inward along the direction perpendicular to the fusion line, while there were mainly equiaxed grains in HAZ due to the relatively small temperature gradient, and its size was still larger than the grain size in the base metal. According to Figure 11b, the base metal showed the presence of both the equiaxed α phase and the intergranular β phase. Combining Figure 11c,d, it was observed that the microstructure in FZ was mainly composed of flaky α and acicular α`, which may be responsible for the higher strength and reduced ductility of FZ, whereas the microstructure in HAZ was dominated by the massive α phase with a small amount of acicular martensite and residual high-temperature β phase. The findings of this investigation about microstructure in FZ and HAZ were consistent with the results of Kumar's study [7].
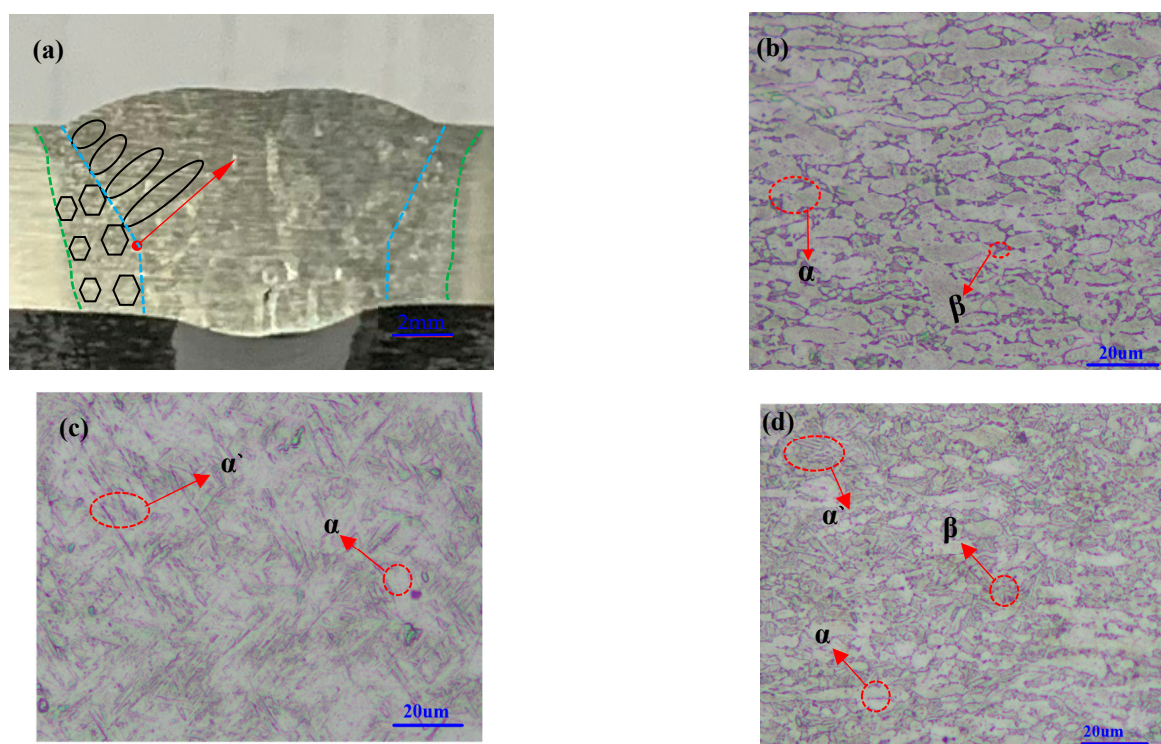

Figure 11. (**a**) Optical micrograph of welding joint; (**b**) microstructure in base metal; (**c**) microstructure in FZ of weldment; and (**d**) microstructure in HAZ of weldment.

4.3. Contour Distribution of Residual Stresses

Contour plots for residual stress after welding are shown in Figures 12 and 13 for the model with and without the effect of SSPT, respectively. In Figure 12b, it can be clearly distinguished that when the effect of SSPT was not considered, the longitudinal residual stresses mainly appeared in the weld and its vicinity and exhibited tensile properties, while the longitudinal residual compressive stresses emerged in the region away from the weld. However, the situation for transverse residual stresses appeared to be different. There was a certain amount of transverse residual compressive stress in the weld and its vicinity, while transverse residual tensile stresses appeared in the region on both sides of the weld. On the other hand, it could be seen from Figure 13a,b that the peak value of the residual stress in the weldments became smaller when the effect of SSPT was considered.
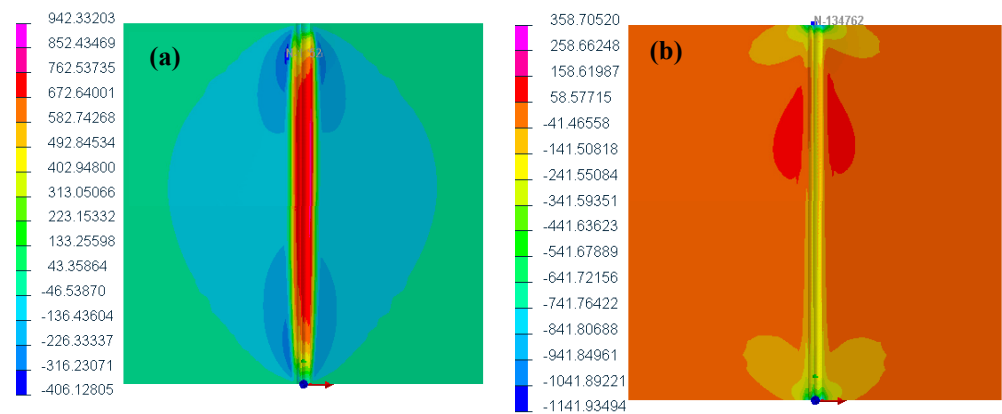
Figure 12. Contour plot of (**a**) longitudinal and (**b**) transverse residual stress distributions after welding without the SSPT effect.
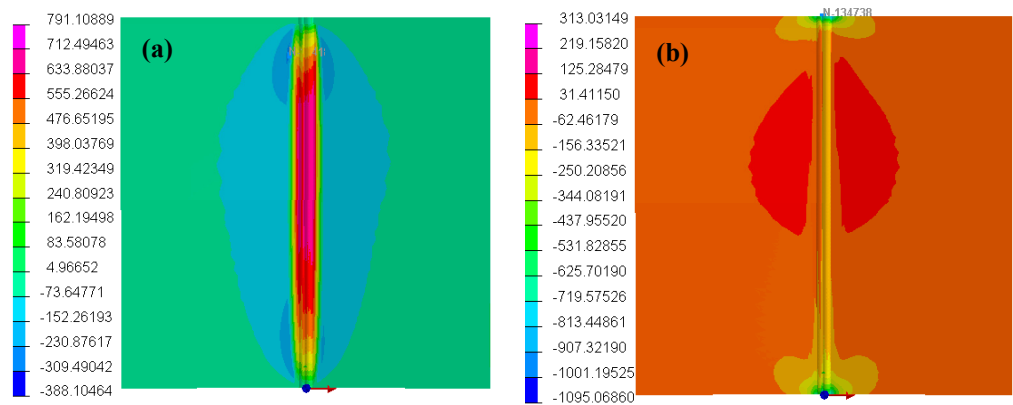

Figure 13. Contour plot of (**a**) longitudinal and (**b**) transverse residual stress distributions after welding with the SSPT effect.

A numerical simulation of the local PWHT with a holding temperature of 700 °C was carried out. The distribution contour plot of the residual stress in the weldments after local PWHT was obtained, as shown in Figure 14a,b. By comparing Figures 13 and 14, it can be clearly seen the peak values of longitudinal and transverse residual stress became significantly smaller after local PWHT, and the distribution of residual stress also changed, indicating the feasibility of the local PWHT to improve the residual stress state in the weldments.
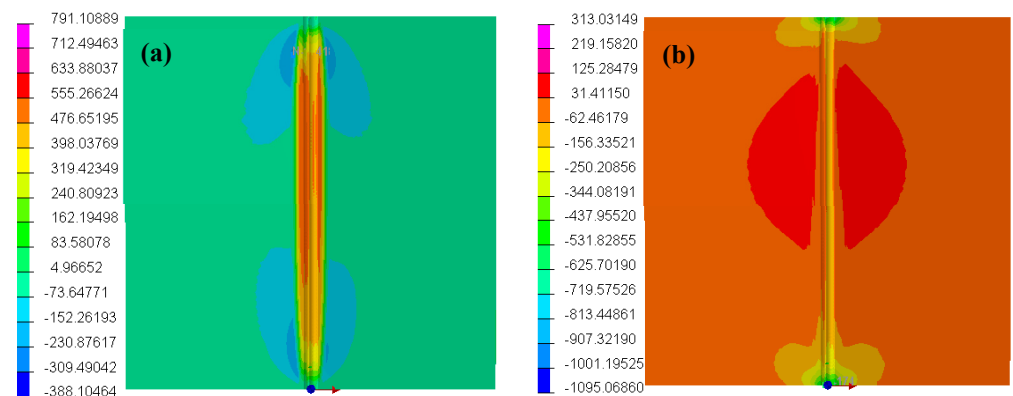

Figure 14. Contour plot of (**a**) longitudinal and (**b**) transverse residual stress distributions after local PWHT.

4.4. Effect of SSPT on Residual Stress at As-Weld State

In order to quantitatively analyze the effect of SSPT on residual stress after welding, the longitudinal residual stress and transverse residual stress on the observation paths 9 and 10 in Figures 12 and 13 were extracted, respectively, as shown in Figures 15 and 16. It could be seen from Figures 15 and 16 that the distribution trends of longitudinal residual stress and transverse residual stress in the weldments were similar when welding with and without SSPT. However, compared to not considering the effect of SSPT, the longitudinal residual tensile stress in the weld, the longitudinal residual compressive stress on both sides of the weld, and the transverse residual compressive stress in the weld became smaller after considering the effect of SSPT, and the peak value of the longitudinal residual stress on the path P9 changed from 774.5 MPa after welding without SSPT to 686.4 MPa after welding with SSPT, a decrease of 12%, which may be attributed to the fact that the volume expansion due to the transformation from β to α ` phase during cooling would release some residual stress. Furthermore, the peak value of transverse residual tensile stress on both sides of the weld was increased. The findings of the current investigation were consistent with the results of other research [28,35].
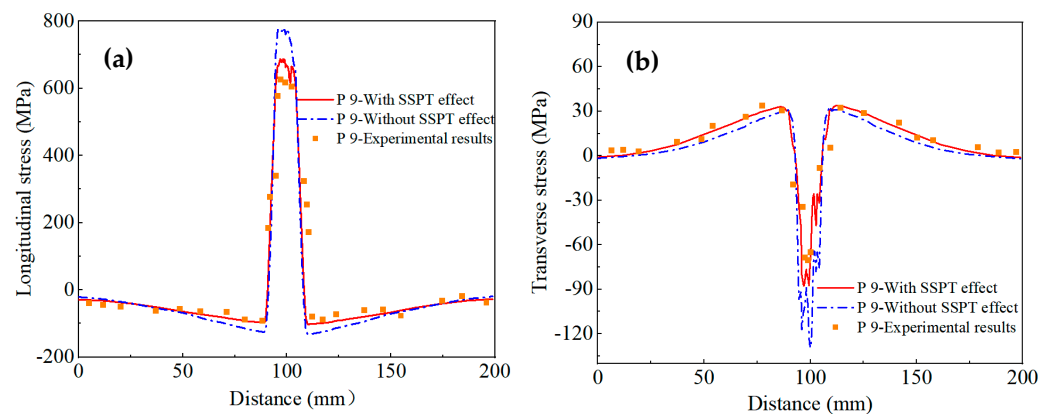

Figure 15. Distribution of (**a**) longitudinal and (**b**) transverse residual stress along path P9 after welding with and without SSPT.
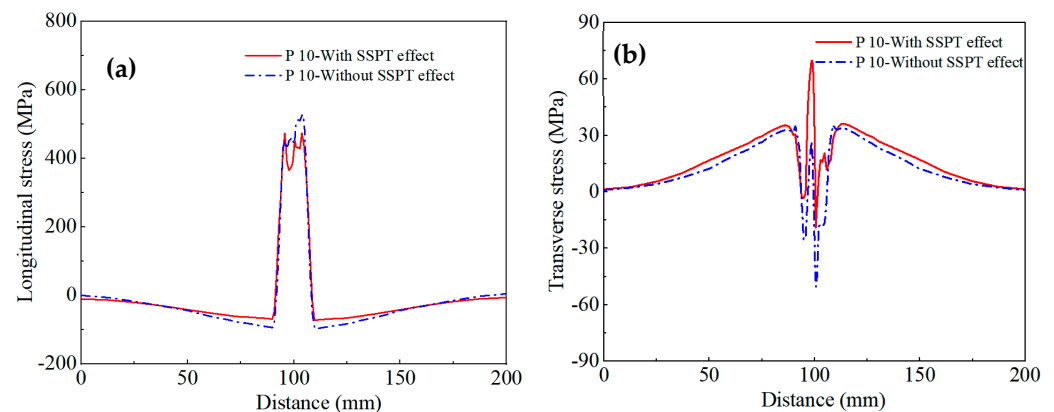

Figure 16. Distribution of (**a**) longitudinal and (**b**) transverse residual stress along path P10 after welding with and without SSPT.

At the same time, it could be found that the influence of the SSPT on the residual stress on observation path 9 was more obvious than that on observation path 10. This phenomenon may be due to the fact that in the multi-layer, multi-pass welding process, the subsequent weld bead filling will reheat the area where path 10 is located, which is equivalent to heat treatment. According to Figure 10b, it can be seen that the martensite in the weld after the heat treatment will be decomposed into α phase and β phase, and

its residual volume fraction is very small, which weakened the expansion of martensite and further reduced the impact of SSPT on the residual stress on the observation path 10. Moreover, the residual stresses on the path P9 obtained by simulation with and without SSPT had a certain deviation from the experimental result, which may be caused by the test error and the simplification of the welding model. However, the simulated results in the case of welding with SSPT were more consistent with the experimental results, indicating that the welding finite element model with SSPT in this work was more accurate. Therefore, the subsequent analyses were based on the welding finite element model, considering the effect of SSPT.

4.5. Effect of Local PWHT on Residual Stress

4.5.1. Residual Stress on the Top Side of the Plate

In order to quantitatively analyze the change of residual stress on the top side of weldments after welding and local PWHT, the residual stresses on the paths P1, P2, P3, P4, and P9 in Figures 13 and 14 were extracted, respectively, as shown in Figures 17 and 18. It could be seen from Figure 17a that the weld and its vicinity on the top side of the weldments presented the longitudinal residual stress as the distance from the weld increased, the residual stresses first became compressive and then became 0 MPa at the edge of the base metal. The peak values of longitudinal residual tensile stress on the observation path P1, path P2, and path P3 were 681.8 MPa, 625.4 MPa, and 337.3 MPa, respectively, while the peak value of longitudinal residual compressive stress on the path P4 was −200 MPa. The reason for the presence of residual stress in the weldments after welding is that the metal material in the molten pool would shrink during cooling and would be restrained by the surrounding metal, resulting in tensile stress in the weld. The resulting tensile stress that does not exceed the yield strength of the material would remain in the weldments, resulting in a larger tensile residual stress in the weld when cooling to room temperature. At the same time, due to the self-balance of the internal stress in the weldments, the longitudinal residual compressive stress will be generated on both sides of the weld, and as the distance from the weld increases, this compressive effect gradually decreases until the longitudinal residual stress on the edge of the base metal approximately becomes 0 MPa.
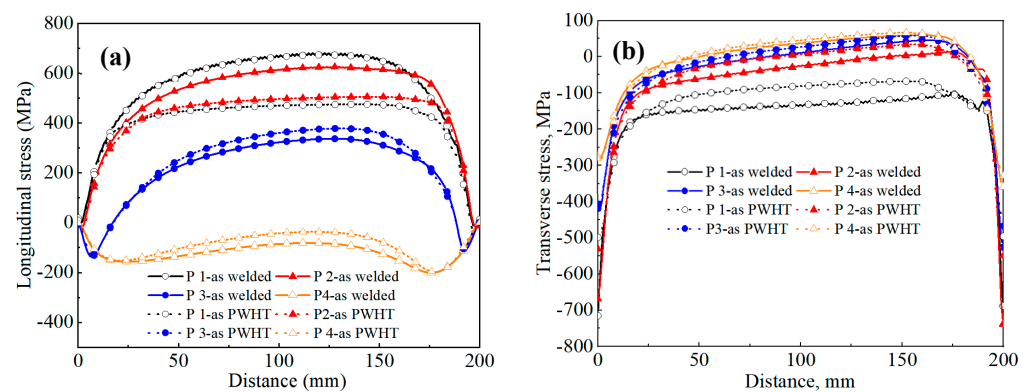

Figure 17. Distribution of (**a**) longitudinal and (**b**) transverse residual stress on the weld surface along the direction of the weld.

Figure 17a also shows that compared with the residual stress on the top side of the weldments after welding, the peak values of longitudinal residual tensile stress on the paths P1 and P2 after local PWHT decreased to 476.3 MPa and 505.1 MPa, which were reductions of 30.1% and 19.2%, respectively. However, the peak value of longitudinal residual tensile stress on the path P3 increased to 378.8 MPa with an increase rate of 12.3%, and the peak value of longitudinal residual compressive stress on the path P4 decreased to −153 MPa, which was a reduction of 23.5%. It could also be found that, compared with the longitudinal residual tensile stress on the path P2, the peak value of the longitudinal residual tensile stress on the path P1 in the center of the weld became smaller and

decreased more greatly. The findings of this investigation about the effect of PWHT on residual stress were consistent with the results of Ren's study [36]. This phenomenon occurs because residual stress is determined by the elastic strain, Young's modulus, and yield strength of the material. During the heat treatment process, the yield strength of the material will decrease with the increase in temperature. When the local residual stress is greater than the yield strength of the material, the material will yield and generate tensile plastic strain, offsetting the compressive plastic strain generated during heating, reducing the elastic strain during cooling, and thereby reducing the residual stress in the area after cooling to room temperature.
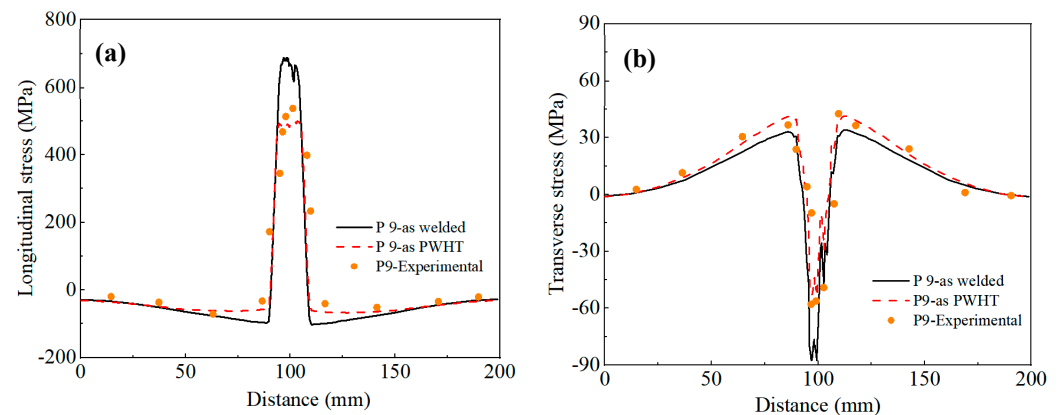

Figure 18. Distribution of (**a**) longitudinal and (**b**) transverse residual stress on the weld surface in the direction perpendicular to the weld.

Figure 18a also shows the same distribution characteristics of residual stress on the top side of weldments as Figure 17a. The reason for the presence of residual stress in the weldments after welding is that the metal material in the molten pool would shrink during the welding cooling process and would be restrained by the surrounding metal, resulting in tensile stress in the weld. The resulting tensile stress that does not exceed the yield strength of the material would remain in the weldments, resulting in a larger tensile residual stress in the weld when the weldments cool to room temperature. At the same time, due to the self-balance of the internal stress in the weldments, the longitudinal residual compressive stress will be generated on both sides of the weld, and as the distance from the weld increases, this compressive effect gradually decreases until the longitudinal residual stress on the edge of the base metal approximately becomes 0 MPa. It could be observed from Figures 17b and 18b that the transverse residual compressive stress on the path P1 after local PWHT became smaller compared with that after welding, while the transverse residual tensile stress in the region away from the weld became bigger, and the amplitude of the increase gradually decreased as the distance from the weld increased. Finally, according to Figure 18, the simulated longitudinal and transverse residual stresses on the path P4 were consistent with the experimental results, further indicating that the welding finite element model was accurate.

4.5.2. Residual Stress on the Bottom Side of the Plate

In order to quantitatively analyze the change in residual stress on the bottom side of the weldments after welding and local PWHT, the residual stresses on the observation paths P5, P6, P7, P8, and P10 in Figures 13 and 14 were extracted, respectively, as shown in Figures 19 and 20. Figure 19a shows that the weld and its vicinity on the bottom side of the weldments were also mainly characterized by large longitudinal residual tensile stresses. The peak values of longitudinal residual tensile stress on paths P5, P6, and P7 were 438 MPa, 433.1 MPa, and 239.7 MPa, respectively, while the peak value of longitudinal residual compressive stress on path P8 was −153.4 MPa.
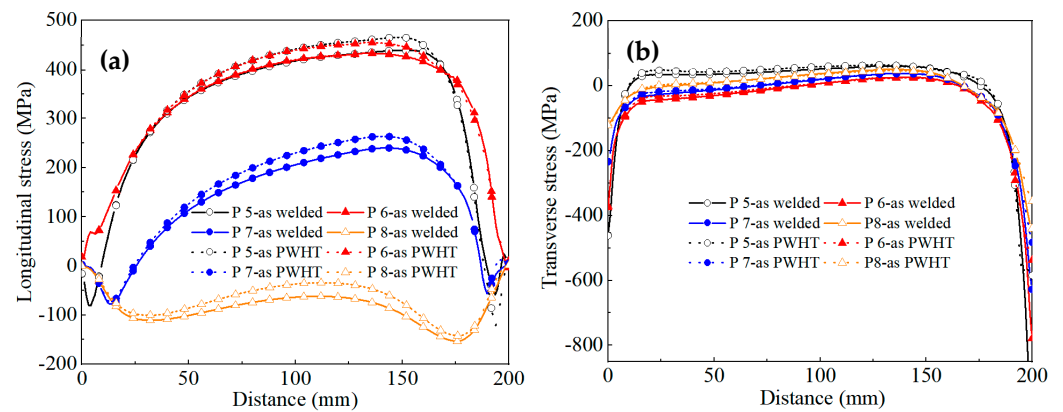
Figure 19. Distribution of (**a**) longitudinal and (**b**) transverse residual stress on the bottom of the weld along the direction of the weld.
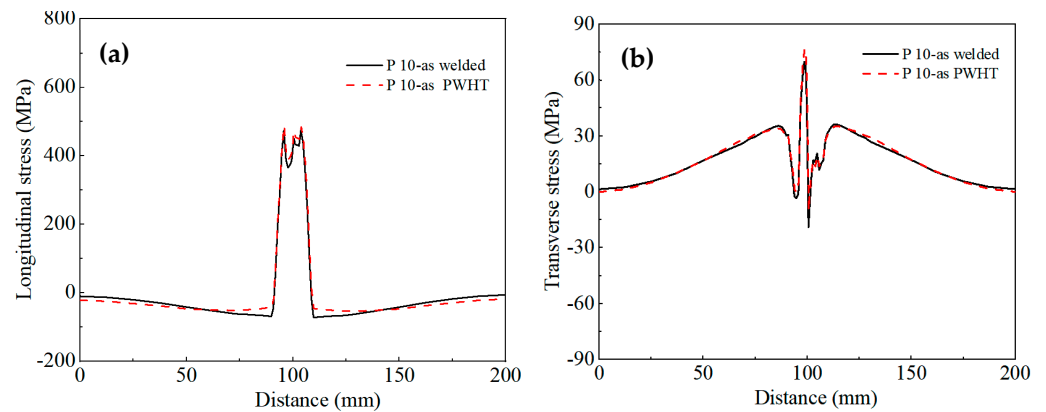

Figure 20. Distribution of (**a**) longitudinal and (**b**) transverse residual stress on the bottom of the weld in the direction perpendicular to the weld.

Figure 19a also shows that the distribution trend of the longitudinal residual stress after local PWHT was similar to that in the as-welded state. However, the peak values of longitudinal residual tensile stress on paths P5, P6, and P7 increased to 465 MPa, 454.4 MPa, and 263.4 MPa with an increase rate of 6.2%, 4.9%, and 9.9%, respectively. The peak value of the longitudinal residual compressive stress on the path P8 was reduced to −100 MPa, which was a reduction of 34.8%. By comparing Figures 17a and 19a, the residual stress at the high-stress region can be released more than that at the low-stress region under local PWHT, and this phenomenon is because the high-stress region is more prone to yielding and producing more tensile plastic deformation compared to the low-stress region, which releases more residual stress. As can be observed in Figures 19b and 20b, the magnitude and distribution of the transverse residual stress on the bottom side of the weldments after local PWHT did not change much compared with that after welding.

4.5.3. Parametric Analysis of PWHT on Residual Stress

Through the analysis in the previous sections, it could be found that local PWHT can effectively reduce the residual stress, especially the longitudinal residual stress in the weld. Thus, the influence of local PWHT parameters on the residual stress ought to be further studied, and the holding time and holding temperature were the important factors that were analyzed. Through the numerical analysis of different cases, the longitudinal residual stresses on the path P1 and the path P9 on the top side of the weldments were obtained under the conditions of different holding times and different holding temperatures, respectively, as shown in Figures 21 and 22.
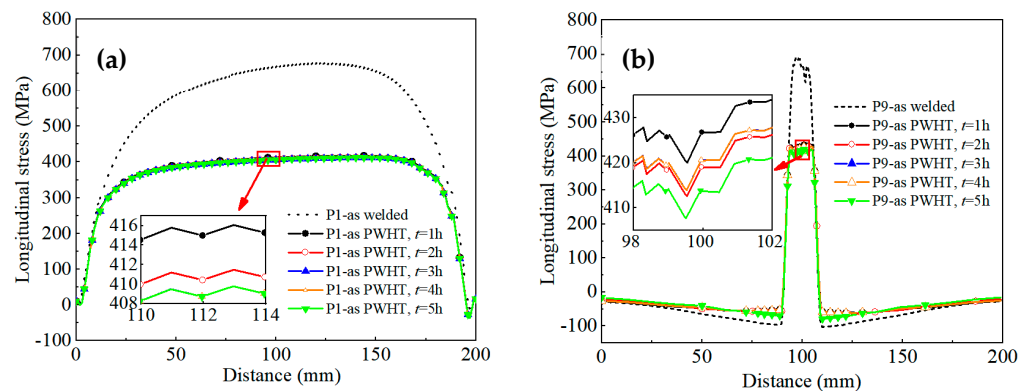
Figure 21. Distribution of (**a**) longitudinal residual stress along the weld direction and (**b**) longitudinal residual stress in the direction perpendicular to the weld at different holding times.
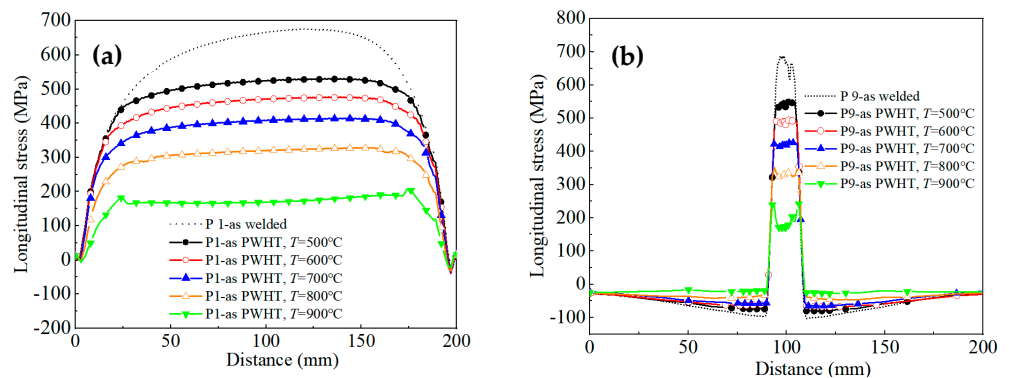

Figure 22. Distribution of (**a**) longitudinal residual stress along the weld direction and (**b**) longitudinal residual stress in the direction perpendicular to the weld at different holding temperatures.

As shown in Figure 21, it could be observed that the holding time had little effect on the release of residual stress, and changing the holding time from 1 h to about 3 h influenced the residual stress relaxation to a greater extent than above 3 h. Figure 22a shows that the effect of holding temperature on the longitudinal residual tensile stress was very obvious. As the holding temperature gradually increased, the longitudinal residual tensile stress decreased more greatly. Compared with the peak value of 681 MPa of longitudinal residual tensile stress on the path P1 after welding, when the holding temperatures were 500 °C, 600 °C, 700 °C, 800 °C, and 900 °C, the peak values of longitudinal residual tensile stress on the path P1 were 530.8 MPa, 476.5 MPa, 414.2 MPa, 327.8 MPa, and 208.3 MPa, and the reductions reached 22.1%, 30%, 39.2%, 51.9%, and 69.4%, respectively. This is because the higher the heat treatment temperature, the smaller the corresponding yield strength of the material, making it easier for the welded part to reach the yield strength of the material and generate greater tensile plastic strain. So, the tensile elastic strain generated during cooling becomes smaller, and the residual stress is released more.

On the other hand, the variation characteristics of residual stress under different holding temperatures in Figure 22b were basically the same as those in Figure 22a, and the peak value of the longitudinal residual stress on the path P9 became 236.4 MPa when the holding temperature was 900 °C, which was 65.6% less than that after welding. In the actual process, it is necessary to take into account the process requirements and production costs to select the appropriate holding temperature for heat treatment, and the heat treatment also has a certain influence on the deformation of the weldments, which will be reported in subsequent studies.

5. Conclusions

In this work, TIG welding of a butt weld in TC4 titanium alloy plates was studied with regard to the thermal cycles, microstructural evolution, and the effect of SSPT and PWHT on residual stress. The findings obtained through numerical methods and experimental measurements can be summarized as follows:

(1) The simulated welding thermal cycles and the shape of the molten pool greatly matched those by experiment, and the peak value of the longitudinal residual stress can reach 686.4 MPa after welding with SSPT, which was 11.38% lower than that without SSPT and was more consistent with that measured by the test, verifying the correctness and feasibility of the simulated model considering the effect of SSPT;

(2) The peak temperature in FZ and HAZ had reached β transus temperature during heating for the last welding pass, and the corresponding maximum cooling rate reached 327 °C/s and 154 °C/s during cooling, respectively, leading to diffusional and diffusionless transformations. After welding, the volume fractions of α in FZ can reach 0.76 but are less than those in the HAZ, while the volume fractions of α` in FZ can reach 0.218 and are more than those in the HAZ;

(3) PWHT will decompose α` into α and β phases and reduce the volume fraction of α` to 0.02 when the heating temperature is 700 °C, making it smaller than that after welding. Moreover, PWHT can effectively reduce and redistribute residual stress in welded joints, and the residual stress peak value decreases by 65.6% from 686.4 MPa after welding to 236.4 MPa when the heating temperature is 900 °C.

References

1. Li, Z.; Zhao, W.; Xiao, G.C.; Chen, K.; Zhang, H.; Guo, N.; Xu, L.Y. Impact of microstructure evolution on the corrosion behaviour of the Ti–6Al–4V alloy welded joint using high-frequency pulse wave laser. *J. Mater. Res. Technol.* **2023**, *24*, 4300–4314. [CrossRef]
2. Liu, H.H.; Aoki, Y.; Aoki, Y.; Aoki, Y.; Ushioda, K.; Fujii, H. Principle for obtaining high joint quality in dissimilar friction welding of Ti-6Al-4V alloy and SUS316L stainless steel. *J. Mater. Res. Technol.* **2020**, *46*, 211–224. [CrossRef]
3. Cheng, H.; Zhou, L.G.; Li, Q.J.; Chang, B.H. Effect of welding parameters on spatter formation in full-penetration laser welding of titanium alloys. *J. Mater. Res. Technol.* **2021**, *15*, 5516–5525. [CrossRef]
4. Wu, Y.H.; Mao, Y.; Fu, L.; Qin, D.Q.; Xiao, X. Dual laser-beam synchronous self-fusion welding of Ti–6Al–4V titanium alloys T-joints based on prefabricated welding materials. *J. Mater. Res. Technol.* **2022**, *17*, 2560–2576. [CrossRef]
5. Xu, M.F.; Chen, Y.H.; Zhang, T.M.; Xie, J.L.; Wang, S.L.; Yin, L.M.; He, P. Microstructure evolution and mechanical properties of wrought/wire arc additive manufactured Ti-6Al-4V joints by electron beam welding. *Mater. Charact.* **2022**, *190*, 112090. [CrossRef]
6. Kumar, K.; Masant, M.; Sahoo, S.K. Microstructure evolution and metallurgical characteristic of bead-on-plate TIG welding of Ti-6Al-4V alloy. *J. Mater. Process. Technol.* **2018**, *265*, 34–43. [CrossRef]
7. Chen, C.; Fan, C.L.; Cai, X.Y.; Lin, S.B.; Liu, Z.; Fan, Q.K.; Yang, C.L. Investigation of formation and microstructure of Ti-6Al-4V weld bead during pulse ultrasound assisted TIG welding. *J. Manuf. Process.* **2019**, *46*, 241–247. [CrossRef]

8. Kumar, C.; Das, M.; Paul, C.P.; Bindra, K.S. Comparison of bead shape, microstructure and mechanical properties of fiber laser beam welding of 2 mm thick plates of Ti-6Al-4V alloy. *Opt. Lase. Technol.* **2018**, *105*, 306–321. [CrossRef]

9. Mehdi, B.; Badji, R.; Ji, V.; Allili, B.; Bradai, D.; Deschaux-Beaume, F.; Soulié, F. Microstructure and residual stresses in Ti-6Al-4V alloy pulsed and unpulsed TIG welds. *J. Mater. Process. Technol.* **2016**, *231*, 441–448. [CrossRef]

10. Etesami, S.A.; Fotovvati, B.; Asadi, E. Heat treatment of Ti-6Al-4V alloy manufactured by laser-based powder-bed fusion: Process, microstructures, and mechanical properties correlations. *J. Alloy. Compd.* **2022**, *895*, 162618. [CrossRef]

11. Bagheri, B.; Abbasi, M.; Hamzeloo, R. Comparison of different welding methods on mechanical properties and formability behaviors of tailor welded blanks (TWB) made from AA6061 alloys. *Proc. Inst. Mech. Eng. Part C J. Mech. Eng. Sci.* **2020**, *235*, 2225–2237. [CrossRef]

12. Nie, G.; Yang, Z.; Zhang, D.; Zhang, X.; Outeiro, J.; Ding, H. Dynamics of chip formation during the cutting process using imaging techniques: A review. *Int. J. Mech. Syst. Dyn.* **2022**, *2*, 27–49. [CrossRef]

13. Chen, Z.H.; Wang, P.; Wang, H.H.; Xiong, Z.L. Thermo-mechanical analysis of the repair welding residual stress of AISI 316L pipeline for ECA. *Int. J. Press. Vessel. Pip.* **2021**, *194*, 104469. [CrossRef]

14. Kumar, A.; Pankaj, P.; Biswas, P.; Rao, A.G. Finite Element Analysis and Experimental Investigation on Effect of Process Parameters in Plasma-Assisted Friction Stir Welding of Low Carbon Steel. *Trans. Indian Inst. Met.* **2022**, *75*, 2559–2579. [CrossRef]

15. Luo, Y.; Jiang, W.C.; Yang, Z.W.; Wang, C.C.; Jin, Q.; Gao, T.; Yan, G.Z.; Tu, S.T.; He, Y.B. Using reinforce plate to control the residual stresses and deformation during local post-welding heat treatment for ultra-large pressure vessels. *Trans. Indian Inst. Met.* **2021**, *191*, 104332. [CrossRef]

16. Hu, L.; Wang, X.; Ma, Q.S.; Meng, W.; Chen, S.S. Numerical and experimental investigations on the temperature field in local post weld heat treatment of 9% Cr heat resistant steel welded pipes. *J. Mater. Process. Technol.* **2021**, *297*, 117232. [CrossRef]

17. Bagheri, B.; Sharifi, F.; Abdollahzadeh, A. On the role of input welding parameters on the microstructure and mechanical properties of Al6061-T6 alloy during the friction stir welding: Experimental and numerical investigation. *Proc. Inst. Mech. Eng. Part L J. Mater. Des. Appl.* **2021**, *236*, 299–318. [CrossRef]

18. Abdollahzadeh, A.; Bagheri, B.; Vaneghi, A.H.; Shamsipur, A.; Mirsalehi, S.E. Advances in simulation and experimental study on intermetallic formation and thermomechanical evolution of Al–Cu composite with Zn interlayer: Effect of spot pass and shoulder diameter during the pinless friction stir spot welding process. *Proc. Inst. Mech. Eng. Part L J. Mater. Des. Appl.* **2022**, *237*, 1475–1494. [CrossRef]

19. Tian, Y.B.; Shen, J.Q.; Hu, S.S.; Wang, Z.J.; Gou, J. Microstructure and mechanical properties of wire and arc additive manufactured Ti-6Al-4V and AlSi5 dissimilar alloys using cold metal transfer welding. *J. Manuf. Process.* **2019**, *46*, 337–344. [CrossRef]

20. Jiang, F.; Fu, Z.Q.; Ji, B.H.; Wan, L. Fatigue life evaluation of deck to U-rib welds in orthotropic steel deck integrating weldment size effects on welding residual stress. *Eng. Fail. Anal.* **2021**, *124*, 105359. [CrossRef]

21. Ahn, J.; He, E.; Chen, L.; Wimpory, R.C.; Dear, J.P.; Davies, C.M. Prediction and measurement of residual stresses and distortions in fibre laser welded Ti-6Al-4V considering phase transformation. *Mater. Des.* **2017**, *115*, 441–457. [CrossRef]

22. Wen, Q.; Ji, S.; Zhan, L.G.; Yue, Y.M.; Lv, Z. Temperature, Stress and Distortion of Ti–6Al–4V Alloy Low-Temperature Friction Stir Welding Assisted by Trailing Intensive Cooling. *Trans. Indian Inst. Met.* **2018**, *71*, 3003–3009. [CrossRef]

23. Zhang, H.; Wang, Y.; Han, T.; Bao, L.; Wu, Q.; Gu, S. Numerical and experimental investigation of the formation mechanism and the distribution of the welding residual stress induced by the hybrid laser arc welding of ah36 steel in a butt joint configuration-sciencedirect. *J. Manuf. Process.* **2020**, *51*, 95–108. [CrossRef]

24. Fisher, C.R.; Bechetti, D.H.; Sinfield, M.F. Comparison of analytical, empirical, and finite-element modeling of weld metal cooling as function of plate orientation, thickness, and heat input. *J. Manuf. Process.* **2021**, *62*, 471–482. [CrossRef]

25. Xian, G.; Yu, J.; Cheepu, M.; Cho, S.M.; Kang, N. Effect of welding speed on microstructure and anisotropic properties of wire-arc additive-manufactured ti-6al-4v alloy. *Trans. Indian Inst. Met.* **2022**, *76*, 483–489. [CrossRef]

26. Buffa, G.; Ducato, A.; Fratini, L. FEM based prediction of phase transformations during Friction Stir Welding of Ti6Al4V titanium alloy. *Mater. Sci. Eng. A-Struct.* **2013**, *851*, 56–65. [CrossRef]

27. Murgau, C.C.; Pederson, R.; Lindgren, L.E. A model for Ti-6Al-4V microstructure evolution for arbitrary temperature changes. *Model. Simul. Mater. Sci. Eng.* **2012**, *20*, 055006. [CrossRef]

28. Kumar, B.; Bag, S. Phase transformation effect in distortion and residual stress of thin-sheet laser welded ti-alloy. *Opt. Laser. Eng.* **2019**, *122*, 209–224. [CrossRef]

29. Sun, J.; Hensel, J.; Klassen, J.; Nitschke-Pagel, T.; Dilger, K. Solid-state phase transformation and strain hardening on the residual stresses in S355 steel weldments. *J. Mater. Process. Technol.* **2019**, *265*, 173–184. [CrossRef]

30. Suman, S.; Biswas, P. Finite element analysis of in- process thermal mitigation of welding induced residual stresses in 9Cr-1Mo-V steel butt joint considering phase transformation. *J. Manuf. Process.* **2021**, *70*, 361–375. [CrossRef]

31. Esmaily, M.; Mortazavi, S.N.; Todehfalah, P.; Rashidi, M. Microstructural characterization and formation of α' martensite phase in ti-6al-4v alloy butt joints produced by friction stir and gas tungsten arc welding processes. *Mater. Des.* **2013**, *47*, 143–150. [CrossRef]

32. Su, J.; Jiang, F.L.; Li, J.J.; Tan, C.L.; Xu, Z.L.; Xie, H.M.; Liu, J.; Tang, J.; Fu, D.F.; Zhang, H.; et al. Phase transformation mechanisms, microstructural characteristics and mechanical performances of an additively manufactured Ti-6Al-4V alloy under dual-stage heat treatment. *Mater. Des.* **2022**, *233*, 111240. [CrossRef]

33. Su, J.; Xie, H.M.; Tan, C.L.; Xu, Z.L.; Liu, J.; Jiang, F.L.; Tang, J.; Fu, D.F.; Zhang, H.; Teng, J. Microstructural characteristics and tribological behavior of an additively manufactured Ti-6Al-4V alloy under direct aging and solution-aging treatments. *Tribol. Int.* **2022**, *175*, 107763. [CrossRef]

34. Galarraga, H.; Warren, R.J.; Lados, D.A.; Dehoff, R.R.; Kirka, M.M.; Nandwana, P. Effects of heat treatments on microstructure and properties of Ti-6Al-4V ELI alloy fabricated by electron beam melting (EBM). *Mater. Sci. Eng. A.* **2017**, *685*, 417–425. [CrossRef]

35. Zhang, K.; Dong, W.; Lu, S. Finite element and experiment analysis of welding residual stress in S355J2 steel considering the bainite transformation. *J. Manuf. Process.* **2021**, *62*, 80–89. [CrossRef]

36. Ren, S.D.; Li, S.; Wang, Y.F.; Deng, D.; Ma, N.S. Finite element analysis of residual stress in 2.25Cr-1Mo steel pipe during welding and heat treatment process. *J. Manuf. Process.* **2019**, *47*, 110–118. [CrossRef]